Table 1. Systematic frequency corrections and their associated uncertainties for the $^1S_0$-$^3P_0$ clock transition, in units of 10^{-16} fractional frequency.

Contributor	Correction (10^{-16})	Uncertainty (10^{-16})
Lattice Stark (scalar/tensor)	−6.5	0.5
Hyperpolarizability (lattice)	−0.2	0.2
BBR Stark	52.1	1.0
ac Stark (probe)	0.2	0.1
First-order Zeeman	0.2	0.2
Second-order Zeeman	0.2	0.02
Density	8.9	0.8
Line pulling	0	0.2
Servo error	0	0.5
Second-order Doppler	0	<<0.01
Systematic total	54.9	1.5

accuracy calculation of the BBR shift considers both bound- and continuum-state contributions, dynamical corrections to the static polarizability, and higher-order multipole contributions (*33*). At room temperature, the uncertainty in the BBR shift originating from uncertainty in the polarizability (1%) is 7×10^{-17}. Further uncertainty in the BBR shift originates from lack of control and homogeneity of the blackbody environment (at room temperature, T). By monitoring many positions on the Sr vacuum chamber, we determine the blackbody environment to $\Delta T = 1$ K (root mean square, contributions from the thermal Sr oven are negligibly small), leading to a shift uncertainty of 7.5×10^{-17}. Combining the two effects yields a 1×10^{-16} total BBR uncertainty.

To further improve the Sr accuracy, the differential static polarizability of the clock states must be known to better than 1% (with the dynamical correction contributing <5% to the total shift). This can be measured directly by enclosing the atoms in a well-characterized blackbody environment and recording the clock shift as this temperature is systematically varied (this simultaneously decreases uncertainty in the BBR environment). The technical challenge lies in the control of temperature homogeneity over various functional areas of the vacuum chamber while accommodating sufficient optical access for a variety of atomic manipulations. One possible solution is to cool and trap atoms in a standard chamber and then transport them in a moving lattice (*34*) to a secondary chamber, where an ideal, well-defined blackbody environment is established (*16*). Such an approach avoids the complexity of cryogenic operation and can be generalized to other lattice clock species. These improvements can potentially improve the BBR-related uncertainty to far below 10^{-16}.

References and Notes
1. T. P. Heavner, S. R. Jefferts, E. A. Donley, J. H. Shirley, T. E. Parker, *Metrologia* **42**, 411 (2005).
2. S. Bize *et al.*, *J. Phys. B* **38**, S449 (2005).
3. L. Hollberg *et al.*, *J. Phys. B* **38**, S469 (2005).
4. M. M. Boyd *et al.*, *Science* **314**, 1430 (2006).
5. W. H. Oskay *et al.*, *Phys. Rev. Lett.* **97**, 020801 (2006).
6. H. S. Margolis *et al.*, *Science* **306**, 1355 (2004).
7. T. Schneider, E. Peik, C. Tamm, *Phys. Rev. Lett.* **94**, 230801 (2005).
8. D. Leibfried, R. Blatt, C. Monroe, D. Wineland, *Rev. Mod. Phys.* **75**, 281 (2003).
9. M. M. Boyd *et al.*, *Phys. Rev. Lett.* **98**, 083002 (2007).
10. Z. W. Barber *et al.*, *Phys. Rev. Lett.* **96**, 083002 (2006).
11. M. Takamoto *et al.*, *J. Phys. Soc. Jpn.* **75**, 104302 (2006).
12. X. Baillard *et al.*, *Eur. Phys. J. D*, published online 7 December 2007; 10.1140/epjd/e2007-00330-3.
13. D. Jaksch, P. Zoller, *Ann. Phys.* **315**, 52 (2005).
14. T. M. Fortier *et al.*, *Phys. Rev. Lett.* **98**, 070801 (2007).
15. S. Schiller *et al.*, *Nuc. Phys. B Proc. Suppl.* **166**, 300 (2007).
16. Additional details are available as supporting material on *Science* Online.
17. S. M. Foreman *et al.*, *Phys. Rev. Lett.* **99**, 153601 (2007).
18. T. Fortier, A. Bartels, S. A. Diddams, *Opt. Lett.* **31**, 1011 (2006).
19. C. W. Oates *et al.*, *IEEE Inter. Freq. Control Symposium and Exposition*, 74 (June 2006).
20. W. M. Itano *et al.*, *Phys. Rev. A* **47**, 3554 (1993).
21. G. Santarelli *et al.*, *IEEE Trans. Ultrason. Ferroelec. Freq. Cont.* **45**, 887 (1998).
22. A. D. Ludlow *et al.*, *Opt. Lett.* **32**, 641 (2007).
23. H. Katori, M. Takamoto, V. G. Pal'chikov, V. D. Ovsiannikov, *Phys. Rev. Lett.* **91**, 173005 (2003).
24. A. D. Ludlow *et al.*, *Phys. Rev. Lett.* **96**, 033003 (2006).
25. A. Brusch, R. Le Targat, X. Baillard, M. Fouche, P. Lemonde, *Phys. Rev. Lett.* **96**, 103003 (2006).
26. M. M. Boyd *et al.*, *Phys. Rev. A* **76**, 022510 (2007).
27. D. E. Chang, J. Ye, M. D. Lukin, *Phys. Rev. A* **69**, 023810 (2004).
28. M. W. Zwierlein, Z. Hadzibabic, S. Gupta, W. Ketterle, *Phys. Rev. Lett.* **91**, 250404 (2003).
29. R. Santra, K. V. Christ, C. H. Greene, *Phys. Rev. A* **69**, 042510 (2004).
30. P. G. Mickelson *et al.*, *Phys. Rev. Lett.* **95**, 223002 (2005).
31. The absolute frequency measurement made over a 48-hour period determined the clock frequency to within a total uncertainty of 8.6×10^{-16}, limited by uncertainties in the NIST maser and F1 Cs fountain operation. The final result agrees with our previous measurement (*9*). For more details, see (*35*).
32. L. Hollberg, J. L. Hall, *Phys. Rev. Lett.* **53**, 230 (1984).
33. S. G. Porsev, A. Derevianko, *Phys. Rev. A* **74**, 020502R (2006).
34. S. Schmid, G. Thalhammer, K. Winkler, F. Lang, J. H. Denschlag, *N. J. Phys.* **8**, 159 (2006).
35. S. Blatt *et al.*, *Phys. Rev. Lett.*, in press; http://arXiv.org/abs/0801.1874.
36. We thank X. Huang for technical help in operating the Sr clock. This research is supported by the Office of Naval Research, National Institute of Standards and Technology, National Science Foundation, and Defense Advanced Research Projects Agency. A.D.L. acknowledges support from NSF-IGERT through the OSEP program at CU. G.K.C. acknowledges support from the National Research Council.

Frequency Ratio of Al⁺ and Hg⁺ Single-Ion Optical Clocks; Metrology at the 17th Decimal Place

T. Rosenband,* D. B. Hume, P. O. Schmidt,† C. W. Chou, A. Brusch, L. Lorini,‡ W. H. Oskay,§ R. E. Drullinger, T. M. Fortier, J. E. Stalnaker,‖ S. A. Diddams, W. C. Swann, N. R. Newbury, W. M. Itano, D. J. Wineland, J. C. Bergquist

Time has always had a special status in physics because of its fundamental role in specifying the regularities of nature and because of the extraordinary precision with which it can be measured. This precision enables tests of fundamental physics and cosmology, as well as practical applications such as satellite navigation. Recently, a regime of operation for atomic clocks based on optical transitions has become possible, promising even higher performance. We report the frequency ratio of two optical atomic clocks with a fractional uncertainty of 5.2×10^{-17}. The ratio of aluminum and mercury single-ion optical clock frequencies ν_{Al^+}/ν_{Hg^+} is 1.052871833148990438(55), where the uncertainty comprises a statistical measurement uncertainty of 4.3×10^{-17}, and systematic uncertainties of 1.9×10^{-17} and 2.3×10^{-17} in the mercury and aluminum frequency standards, respectively. Repeated measurements during the past year yield a preliminary constraint on the temporal variation of the fine-structure constant α of $\dot{\alpha}/\alpha = (-1.6 \pm 2.3) \times 10^{-17}$/year.

Time is the physical coordinate over which humans have the least control, and yet it is the most accurately realized fundamental unit. Although any physical system that

evolves predictably can serve as a time base, isolated atoms have long been recognized as near-ideal references for laboratory clocks, due to the abundance of identical copies, as well as their

relative immunity to environmental changes. Because the forces within isolated atoms are many orders of magnitude larger than the external forces perturbing them, atomic resonance frequencies are affected only slightly by external fields. Yet even the small perturbations caused by external fields limit the accuracy of all atomic clocks.

In the work reported here, we combine recent advances in optical and atomic physics to construct atomic clocks based on optical transitions in trapped ^{199}Hg$^+$ and ^{27}Al$^+$ ions, and measure their frequency ratio. Quantum-jump spectroscopy of single ions (1, 2) and subhertz lasers (3, 4), together with the femtosecond laser frequency comb (5, 6), allowed the first demonstration of an all-optical atomic clock (7), which was based on ^{199}Hg$^+$. The development of quantum logic spectroscopy (8) has enabled the use of ^{27}Al$^+$ as a frequency standard (9), an ion that is highly immune to external field perturbations (10), but whose internal state is difficult to detect by conventional methods.

In each of the standards, the frequency that we attempt to produce in the laboratory is the resonance frequency of the unperturbed ion, at rest and in the absence of background electric and magnetic fields. The deviations from this ideal condition produce shifts that are subtracted from the frequencies of two standards, to the degree that they are known (Table 1). The overall uncertainty in these shifts determines the final accuracy of each frequency standard. Although the specifics of the two standards are quite different, their respective systematic fractional frequency uncertainty is similar: 1.9×10^{-17} for ^{199}Hg$^+$ and 2.3×10^{-17} for ^{27}Al$^+$. Importantly, none of the current uncertainties are fundamental limits, and both standards can be improved substantially in the future, with a potential accuracy of 10^{-18} or better (1, 11). The ratio of frequencies for the two optical clocks ν_{Al^+}/ν_{Hg^+} reported here marks an order-of-magnitude improvement in achievable measurement accuracy (12). As each of these clocks has an accuracy that exceeds current realizations of the SI unit of time, we report the ratio of these optical frequencies, thereby avoiding the uncertainty (3.3×10^{-16}) of the currently realized SI second (13).

Until recently, such an optical frequency–ratio measurement (Fig. 1) would have required large and costly frequency-multiplication chains to translate between the microwave domain of electronic frequency counters and the optical domain of the clock resonances. The development of tabletop femtosecond laser frequency combs

(femtosecond combs) allows this translation to occur in a single, phase-coherent, convenient, and robust step. Here, the fourth harmonics of two clock lasers are locked to the mercury and aluminum clock transitions at 282 and 267 nm, respectively. An octave-spanning self-referenced Ti:Sapphire femtosecond comb (14) is phase-locked to one clock laser, and the heterodyne beat-note of the other clock laser with the nearest comb tooth is measured. The various beat-note and offset frequencies are combined to yield the unitless frequency ratio (12). In recent comparisons of the frequencies of the two optical clocks described here, a fiber laser femtosecond comb (15) has provided a second independent measure of the frequency ratio.

The ^{27}Al$^+$ $^1S_0 \leftrightarrow ^3P_0$ standard, which uses quantum logic spectroscopy (8), has been described previously (9). One ^{27}Al$^+$ ion is trapped together with a ^{9}Be$^+$ ion, which provides sympathetic Doppler laser cooling as well as the means for internal-state detection of the ^{27}Al$^+$ ion's clock state ($^1S_0$ or $^3P_0$). The ^{27}Al$^+$ clock state is mapped to detectable states in ^{9}Be$^+$ repetitively through the ions' coupled motion, allowing for up to 99.94% clock state detection fidelity (16). With the ability to detect the clock state comes the ability to detect state transitions, whose probability depends on the clock laser frequency. The frequency of the clock laser is locked to the atomic transition by alternating between upper and lower slopes of the atomic resonance curve and applying frequency-feedback

Table 1. ^{27}Al$^+$ $^1S_0 \leftrightarrow ^3P_0$ and ^{199}Hg$^+$ $^2S_{1/2} \to ^2D_{5/2}$ clock shifts ($\Delta\nu$), and uncertainties (σ) in units of 10^{-18} of fractional frequency. AOM, Accousto-optic modulator.

| Shift	$\Delta\nu_{Al}$	σ_{Al}	$\Delta\nu_{Hg}$	σ_{Hg}	Limitation
Micromotion	−20	20	−4	4	Static electric fields
Secular motion	−16	8	−3	3	Doppler cooling
Blackbody radiation	−12	5	0	0	DC polarizability
313-nm Stark	−7	2	–	–	Polarizability, intensity
DC quadratic Zeeman	−453	0.5	−1130	5	B-field calibration
AC quadratic Zeeman	0	1	0	10	Trap RF B-fields
Electric quadrupole	0	0.5	0	10	B-field orientation
First-order Doppler	0	1	0	7	Statistical imbalance
Background gas collisions	0	0.5	0	4	Collision model
AOM phase chirp	0	0.1	0	6	RF power
Gravitational red-shift	−5	1	–	–	Clock height
Total	−513	23	−1137	19	
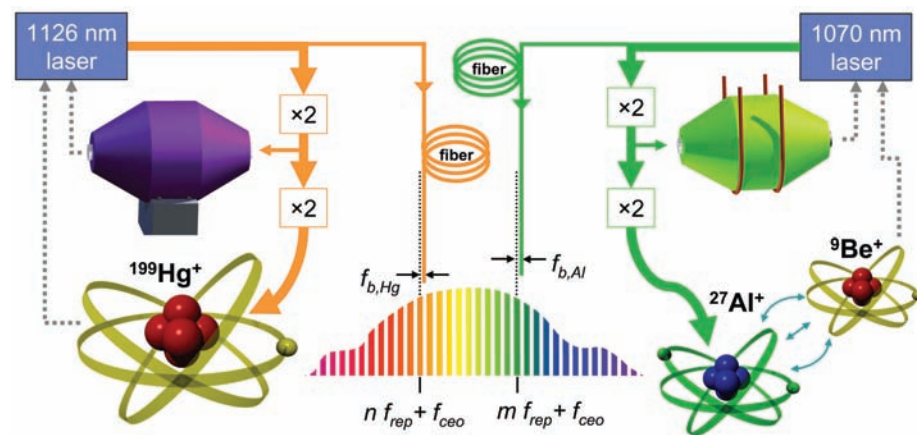
Fig. 1. Frequency ratio measurement system for the comparison of ^{199}Hg$^+$ and ^{27}Al$^+$ optical clock frequencies. (Left) The fourth harmonic of a 1126-nm wavelength infrared (IR) laser drives atomic-state transitions in a ^{199}Hg$^+$ ion (40-ms probe time, 70% duty cycle). The transition rate yields an error signal to keep the laser frequency locked to the atomic resonance. (Right) A 1070-nm wavelength IR laser performs the same function for ^{27}Al$^+$ (100-ms probe time, 45% duty cycle), which is coupled to a nearby ^{9}Be$^+$ ion by their mutual Coulomb repulsion for the purposes of sympathetic cooling and internal state detection. Both lasers are prestabilized to ultralow-expansion glass Fabry-Perot cavities (purple and green ellipsoids), thereby narrowing their linewidth to about 1 Hz (4). Boxes marked "×2" are second-harmonic generation stages to convert IR light first to visible and then to ultraviolet wavelengths. The two laser frequencies are compared by means of a femtosecond comb (12), to which both clock laser systems are linked by 300-m lengths of actively phase-stabilized optical fiber. The quantities $f_{b,Hg}$ (beat note of the mercury clock laser with spectral component n of femtosecond comb), $f_{b,Al}$ (beat note of the aluminum clock laser with spectral component m of the femtosecond comb), f_{ceo} (femtosecond comb carrier-envelope-offset), and f_{rep} (femtosecond comb repetition rate) comprise the frequency ratio measurement (12).

National Institute of Standards and Technology, 325 Broadway, Boulder, CO 80305, USA.

*To whom correspondence should be addressed. E-mail: trosen@boulder.nist.gov

†Present address: Institut für Experimentalphysik, Universität Innsbruck, Austria.

‡Present address: Istituto Nazionale di Ricerca Metrologica (INRIM), Torino, Italy.

§Present address: Stanford Research Systems, Sunnyvale, CA 94089, USA.

‖Present address: Department of Physics and Astronomy, Oberlin College, Oberlin, OH 44074, USA.

to keep the transition rates equal. At the operating magnetic field of 0.1 mT, the Zeeman structure due to the nuclear spin of 5/2 is split by several kilohertz, and the individual Zeeman components are well resolved. The clock alternates every 4 s between π-polarized transitions with extreme states of opposite angular momentum ($m_F = \pm 5/2$), which allows compensation of magnetic field shifts to first and second order (9, 17).

The accuracy of the aluminum standard is limited to 2.3×10^{-17} (Table 1), due primarily to uncertainties in the relativistic time dilation, or second-order Doppler shift, caused by microscopic movement of the ion in its trap, with root mean square (RMS) velocities of $v = 1$ to 2 m/s. According to special relativity, moving clocks are observed to run more slowly than stationary ones, with a fractional frequency shift of $-v^2/(2c^2)$. For ions confined in Paul traps, there are two types of motion: secular motion, which is the harmonic motion of the trapped particle, and micromotion, which occurs in part when the ion is displaced from the null of the radiofrequency (RF) confining field by slowly fluctuating electric fields.

These quasistatic fields are monitored and nulled by interleaving micromotion test experiments with the clock interrogations. Tests are performed by measuring the strength of radial-to-axial coupling of certain normal modes via $^9Be^+$ (18); nulling is accomplished by applying compensation potentials at the ion trap to minimize this coupling. With real-time corrections, the stray electric fields are nulled to (0 ± 10) V/m, allowing an estimate of the time-dilation shift and uncertainty (19). The clock shift depends quadratically on the uncompensated electric field, and in the extreme case of a 10-V/m field along both radial directions, the fractional frequency shift is -3.2×10^{-17}. We estimate the shift caused by such residual electric fields to be $(-2 \pm 2) \times 10^{-17}$ when the clock is operating.

Secular mode heating (20, 21) causes deviations in the secular kinetic energy from the Doppler-cooling limit. We apply 313-nm $^9Be^+$ Doppler-cooling light continuously during each 100-ms clock-transition interrogation, to keep the $^{27}Al^+/^9Be^+$ ion pair as cold as possible. However, two poorly damped normal modes of motion heat the ion above the Doppler-cooling limit during this time (12), which leads to a second-order Doppler shift of $(-1.6 \pm 0.8) \times 10^{-17}$. Other important shifts are the blackbody radiation shift, which is very small in $^{27}Al^+$ (10), and the DC quadratic Zeeman shift, which has been accurately calibrated by varying the magnetic field and measuring the shift in the $^{27}Al^+/^{199}Hg^+$ frequency ratio together with the linear Zeeman splitting v_1 between the ($^1S_0$ F = 5/2, $m_F = \pm 5/2$) ↔ ($^3P_0$ F = 5/2, $m_F = \pm 5/2$) lines. The resulting shift is $v_2 = -v_1^2 \times 1.0479(7) \times 10^{-8}$ Hz^{-1} = $-7.1988(48) \times 10^7$ Hz/T^2.

The $^{199}Hg^+$ ion standard is based on the ($^2S_{1/2}$ F = 0) → ($^2D_{5/2}$ F = 2, $m_F = 0$) electric-quadrupole transition (22). A 194-nm laser cools the ion to the Doppler-cooling limit via the allowed $^2S_{1/2} → ^2P_{1/2}$ transition, and a fiber clock laser frequency-quadrupled to 282 nm excites the clock transition. The clock state of the $^{199}Hg^+$ ion is measured directly via quantum jumps in the scattering fluorescence rate of the 194-nm laser (2). Systematic uncertainties in the $^{199}Hg^+$ standard are listed in Table 1 and have been described previously (22, 23). The dominant uncertainties are due to the quadratic Zeeman effect and the electric quadrupole shift. The AC quadratic Zeeman uncertainty stems from possible unbalanced RF currents in the ion trap. The magnitude of this shift is conservatively estimated by assuming a worst-case asymmetry of 50% in the RF currents that flow in the nominally symmetric ion trap. Such an asymmetry would produce an RMS field of ~7.3×10^{-7} T at the ion (12), causing a fractional frequency shift of -1.0×10^{-17}. We use this value as an upper bound for the magnitude of the shift. The electric-quadrupole shift, which has previously limited the accuracy of the $^{199}Hg^+$ standard, is constrained below 10^{-17} by averaging over three orthogonal magnetic field directions (23, 24).
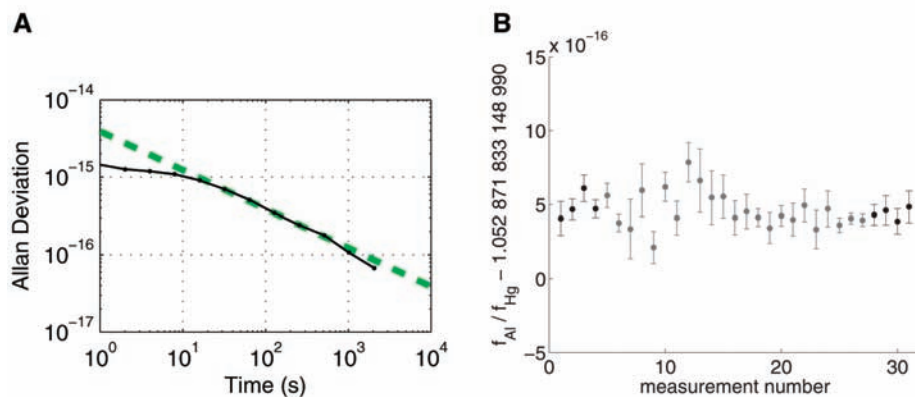

Fig. 2. (A) Allan deviation of a frequency comparison measurement (11,000 s total). The dashed line represents a $1/\sqrt{\tau}$ slope, beginning at 3.9×10^{-15} for 1 s. **(B)** History of frequency ratio measurements of the $^{199}Hg^+$ and $^{27}Al^+$ frequency standards. Error bars are statistical. Only the last four points are used in the ratio reported here (Fig. 3).
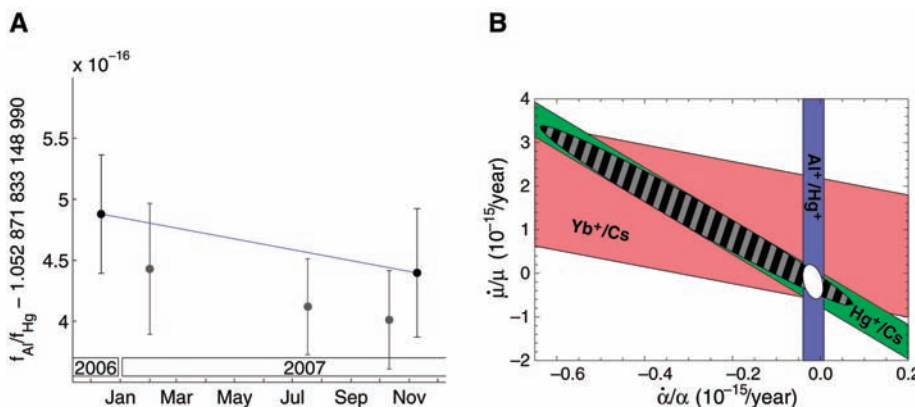

Fig. 3. (A) History of frequency ratio measurements grouped by month. The line connects the first point to the last one with a slope of $(-5.3 \pm 7.9) \times 10^{-17}$/year. Lightly shaded points represent measurements where various systematic shifts were not verified to be at the level stated in Table 1 at the time of the measurements. In the first point, the first-order Doppler shift was not monitored, but all other shifts were well controlled. We do not expect this point to have an error due to this effect, because neither apparatus has ever shown a first-order Doppler shift. For the last point, all shifts listed in Table 1 were well controlled. Error bars are a combination of the statistical measurement uncertainty, and the systematic uncertainties listed in Table 1. **(B)** Preliminary constraint on temporal variation of fine-structure constant α from this measurement (vertical bar). The horizontal axis corresponds to variation of the fine-structure constant, and the vertical axis corresponds to variation of the cesium nuclear magnetic moment $\mu = \mu_{Cs}/\mu_B$ in units of the Bohr magneton μ_B, which is not constrained by this measurement. Also shown are laboratory constraints due to $^{199}Hg^+$ versus Cs (33) and $^{171}Yb^+$ versus Cs (34) measurements. The striped ellipse represents the standard uncertainty for the temporal variation of α and μ due to these previous comparisons of atomic clocks, and the smaller white ellipse shows the reduced uncertainty when the present result is combined with the earlier data. This ellipse constrains $\dot{\mu}/\mu$ to $(-1.9 \pm 4.0) \times 10^{-16}$/year.

Second-order Doppler shifts for ^{199}Hg$^+$ are easier to control than for ^{27}Al$^+$, because the heavy mercury ion moves less in response to ambient electric fields than the lighter aluminum ion does. Near the Doppler-cooling limit, the total time-dilation shift due to secular motion is $(-3 \pm 1) \times 10^{-18}$. Micromotion is carefully compensated [19], leading to a shift of $(-4 \pm 4) \times 10^{-18}$. Thermal blackbody radiation has a negligible effect on the ^{199}Hg$^+$ ion, which operates in a cryogenic environment of 4 K [23]. The quadratic Zeeman coefficient in ^{199}Hg$^+$ was calibrated in a way analogous to that of the ^{27}Al$^+$ standard. Here the shift is $\nu_2 = -\nu_1^2 \times 4.9465(29) \times 10^{-11}$ Hz$^{-1} \approx -1.89 \times 10^{10}$ Hz/T^2, where ν_1 is the linear Zeeman splitting between the $(^2S_{1/2}\ F = 0) \rightarrow (^2D_{5/2}\ F = 2,\ m_F = \pm 1)$ lines.

First-order Doppler shifts from photon-recoil are suppressed in tightly bound atomic particles [25], due to the Mössbauer effect, where each photon-absorption event lasts for many motional-oscillation cycles. Trapped ions [1, 2] and neutral atoms in optical lattices [26] benefit from this effect, but first-order Doppler shifts may still occur, if the trap itself moves in a correlated fashion with the clock laser pulses. Possible causes for such a shift in ion traps might be stray charge buildup from photo-electrons, which are correlated with the interrogation pulses, or more generally, correlated mechanical motion caused by thermal transients or optical shutters. A correlated velocity of only 10^{-8} m/s would cause a first-order Doppler shift error of 3×10^{-17}. Both standards were evaluated for first-order Doppler shifts by illuminating the ions with counter-propagating clock-laser beams, allowing such motion to be both detected and averaged away. The probe direction is selected by shifting the opposite laser beam away from the ion's resonance, either spectrally by ± 100 kHz, in the case of ^{27}Al$^+$ (several times per second), or spatially by a few beam waists in the ^{199}Hg$^+$ clock (every hour). We have not observed a direction-dependent shift in either standard. However, the ratio reported here contains unequal statistical weights for the two probe directions in the ^{199}Hg$^+$ standard. This leads to an additional uncertainty of 7×10^{-18} [12], which we treat as a systematic uncertainty in the ^{199}Hg$^+$ standard (Table 1).

The ^{199}Hg$^+$ and ^{27}Al$^+$ atomic clocks were operated simultaneously, while the femtosecond combs recorded their frequency ratio every second. Figure 2A shows the Allan deviation (an estimate of the statistical measurement uncertainty versus measurement duration) of a typical ratio measurement. For measurement durations τ greater than 100 s, the deviation is given by $3.9 \times 10^{-15}/\sqrt{\tau/s}$. A departure from this slope at long measurement times, which would indicate fluctuating systematic shifts, has not been observed. We expect that both clocks contribute uncorrelated noise of approximately equal magnitude to the statistical measurement uncertainty and derive a long-term stability of $2.8 \times 10^{-15}/\sqrt{\tau/s}$ for each clock.

Figures 2B and 3A show the history of measurements of the ν_{Al^+}/ν_{Hg^+} ratio. Although the first-order Doppler evaluation discussed in the previous paragraph was carried out fully only for the last four data points of Fig. 2B (which, when combined, give the last point of Fig. 3A), the consistency of the earlier measurements provides confidence in the reproducibility of this result. These four points result in a weighted mean of $\nu_{Al^+}/\nu_{Hg^+} = 1.052871833148990438(55)$, where the statistical uncertainty of 4.3×10^{-17}, the ^{27}Al$^+$ systematic uncertainty of 2.3×10^{-17}, and the ^{199}Hg$^+$ systematic uncertainty of 1.9×10^{-17} have been added in quadrature, to yield a fractional ratio uncertainty of 5.2×10^{-17}. This ratio may be multiplied by the ^{199}Hg$^+$ absolute frequency, which was calibrated by the NIST-F1 primary cesium standard [27], to yield a frequency of 1121015393207857.4(7) Hz for the ^{27}Al$^+$ standard.

Previous tests for possible counting errors or systematic offsets in the optical frequency combs have shown that the techniques used here support fractional uncertainties on the order of 10^{-19} [28, 29]. Further details are provided in the supporting online materials [12]. As an additional check, for many of the measurements of Fig. 2B, an independent Er:fiber-based comb [15] measured ν_{Al^+}/ν_{Hg^+} simultaneously with the Ti:sapphire femtosecond comb [14]. During the last four measurements of Fig. 2B, these measurements show agreement at the level of 1.3×10^{-17}, which is consistent with the nonoverlapping dead-time fractions of 3% and 5% in the frequency counters used by the two independent femtosecond combs. This dead-time error is already included in the statistical measurement uncertainty of 4.3×10^{-17}.

The last entry in Table 1, the gravitational redshift uncertainty of the ^{27}Al$^+$ clock with respect to the ^{199}Hg$^+$ clock, is only 10^{-18}, because the two standards are in adjacent laboratories, and their height difference was easily measured with 1-cm uncertainty. This uncertainty is typically much larger for greater separations and, for example, contributes 3×10^{-17} uncertainty for intercontinental primary-standard comparisons between Boulder, Colorado, USA, and other locations [30]. In the future, high-accuracy portable optical clocks may be available, which could be used to map the height of the geoid with an accuracy beyond that achievable from satellite-based geodesy. Such an endeavor would also require an improved frequency-transfer link between a stationary reference clock and the distant portable standard.

Besides their application to frequency metrology and precision time-keeping, accurate atomic clocks can also help address a fundamental question in physics: Are the constants of nature really constant, or do they change in time or depend on the gravitational potential in which they are measured? Frequency ratio measurements of dissimilar atomic clocks can help answer these questions, because these ratios depend on the fine-structure constant α. From the sequence of measurements in Fig. 3A, one may extract a linear rate of change in the frequency ratio of $(-5.3 \pm 7.9) \times 10^{-17}$/year. A fractional change in α of δ leads to a fractional shift of -3.19δ in the energy of the ^{199}Hg$^+$ clock transition when it is expressed in units of the Rydberg energy [31]. For ^{27}Al$^+$, the fractional shift is 0.008δ [32]. Thus, the measured linear slope in the frequency ratio corresponds to $\dot{\alpha}/\alpha = (-1.6 \pm 2.3) \times 10^{-17}$/year, consistent with no change (Fig. 3B). However, due to the absence of first-order Doppler shift tests in the first point (Fig. 3 legend), this result must be considered preliminary.

The uncertainties in the atomic clocks reported here occur at the exciting intersection of relativity, geodesy, and quantum physics, and the total uncertainty of 5.2×10^{-17} shows unprecedented sensitivity to gravitational effects and cosmological fluctuations. Future improvements in these atomic clocks will provide even more sensitive probes of nature.

References and Notes

1. H. G. Dehmelt, *IEEE Trans. Instrum. Meas.* **31**, 83 (1982).
2. J. C. Bergquist, W. M. Itano, D. J. Wineland, *Phys. Rev. A* **36**, 428 (1987).
3. C. Salomon, D. Hils, J. L. Hall, *J. Opt. Soc. Am. B* **5**, 1576 (1988).
4. B. C. Young, F. C. Cruz, W. M. Itano, J. C. Bergquist, *Phys. Rev. Lett.* **82**, 3799 (1999).
5. T. W. Hänsch, *Rev. Mod. Phys.* **78**, 1297 (2006).
6. J. L. Hall, *Rev. Mod. Phys.* **78**, 1279 (2006).
7. S. A. Diddams *et al.*, *Science* **293**, 825 (2001).
8. P. O. Schmidt *et al.*, *Science* **309**, 749 (2005).
9. T. Rosenband *et al.*, *Phys. Rev. Lett.* **98**, 220801 (2007).
10. T. Rosenband *et al.*, http://arxiv.org/abs/physics/0611125.
11. D. J. Wineland, W. M. Itano, J. C. Bergquist, R. G. Hulet, *Phys. Rev. A* **36**, 2220 (1987).
12. Additional supporting materials are available at *Science* Online.
13. S. R. Jefferts, T. P. Heavner, T. E. Parker, J. H. Shirley, *Proc. SPIE* **6673**, 667309 (2007); available at http://tf.nist.gov/timefreq/general/pdf/2254.pdf.
14. T. M. Fortier, A. Bartels, S. A. Diddams, *Opt. Lett.* **31**, 1011 (2006).
15. W. C. Swann *et al.*, *Opt. Lett.* **31**, 3046 (2006).
16. D. B. Hume, T. Rosenband, D. J. Wineland, *Phys. Rev. Lett.* **99**, 120502 (2007).
17. J. E. Bernard, L. Marmet, A. A. Madej, *Opt. Commun.* **150**, 170 (1998).
18. M. D. Barrett *et al.*, *Phys. Rev. A* **68**, 042302 (2003).
19. D. J. Berkeland, J. D. Miller, J. C. Bergquist, W. M. Itano, D. J. Wineland, *J. Appl. Phys.* **83**, 5025 (1998).
20. Q. A. Turchette *et al.*, *Phys. Rev. A* **61**, 063418 (2000).
21. L. Deslauriers *et al.*, *Phys. Rev. Lett.* **97**, 103007 (2006).
22. W. H. Oskay *et al.*, *Phys. Rev. Lett.* **97**, 020801 (2006).
23. W. M. Itano, *J. Res. NIST* **105**, 829 (2000).
24. W. H. Oskay, W. M. Itano, J. C. Bergquist, *Phys. Rev. Lett.* **94**, 163001 (2005).
25. R. H. Dicke, *Phys. Rev.* **89**, 472 (1953).
26. H. Katori, M. Takamoto, V. G. Pal'chikov, V. D. Ovsiannikov, *Phys. Rev. Lett.* **91**, 173005 (2003).
27. J. E. Stalnaker *et al.*, *Appl. Phys. B* **89**, 167 (2007).
28. L.-S. Ma *et al.*, *Science* **303**, 1843 (2004).
29. I. Coddington *et al.*, *Nat. Photonics* **1**, 283 (2007).
30. N. K. Pavlis, M. A. Weiss, *Metrologia* **40**, 66 (2003).
31. V. A. Dzuba, V. V. Flambaum, J. K. Webb, *Phys. Rev. A* **59**, 230 (1999).
32. E. J. Angstmann, V. A. Dzuba, V. V. Flambaum, *Phys. Rev. A* **70**, 014102 (2004).
33. T. M. Fortier *et al.*, *Phys. Rev. Lett.* **98**, 070801 (2007).

34. E. Peik *et al.*, http://arxiv.org/abs/physics/0611088v1.
35. We thank C. W. Oates, M. A. Lombardi, and D. R. Smith for comments on the manuscript and K. Feder, J. Nicholson, and P. Westbrook for specialty nonlinear fiber used in the fiber frequency comb. This work was supported by the Office of Naval Research, Disruptive Technology Office, and NIST. P.O.S. acknowledges

Self-Assembly of Large and Small Molecules into Hierarchically Ordered Sacs and Membranes

Ramille M. Capito,[1] Helena S. Azevedo,[1,2] Yuri S. Velichko,[3] Alvaro Mata,[1] Samuel I. Stupp[1,3,4,5]*

We report here the self-assembly of macroscopic sacs and membranes at the interface between two aqueous solutions, one containing a megadalton polymer and the other, small self-assembling molecules bearing opposite charge. The resulting structures have a highly ordered architecture in which nanofiber bundles align and reorient by nearly 90° as the membrane grows. The formation of a diffusion barrier upon contact between the two liquids prevents their chaotic mixing. We hypothesize that growth of the membrane is then driven by a dynamic synergy between osmotic pressure of ions and static self-assembly. These robust, self-sealing macroscopic structures offer opportunities in many areas, including the formation of privileged environments for cells, immune barriers, new biological assays, and self-assembly of ordered thick membranes for diverse applications.

The organization of molecules at interfaces has been a phenomenon of great interest over the past few decades given its importance in the preparation of chemically defined surfaces and ordered materials. One classical system is the Langmuir-Blodgett film in which molecules are ordered by compression at an air-water interface, followed by deposition of multilayers through repeated immersion of a solid substrate into the liquid phase (*1–3*). Another widely studied system is the self-assembling monolayer formed at a solid-liquid interface by the reaction and self-ordering of dissolved molecules on a solid surface (*4, 5*). Other systems include the formation of molecular complexes or solid objects at the interface of two immiscible liquids (*6, 7*), and electrostatic layer-by-layer deposition of amorphous polymers at the solid-liquid interface through alternation of their charge (*8*).

We report the self-assembly of ordered materials well beyond the monolayer scale at an aqueous liquid-liquid interface. We combined a 1 to 2 weight (wt) % peptide amphiphile (PA) solution with a 0.5 to 2 wt% solution of the high molecular weight polysaccharide hyaluronic acid (HA) (fig. S1A). PAs are small synthetic molecules containing typically a hydrophobic alkyl segment covalently grafted to a short peptide. The one used here consisted of an alkyl tail of 16 carbons attached to the peptide sequence $V_3A_3K_3$ (fig. S1B). We previously developed a broad class of PAs that are known to self-assemble into high aspect ratio nanofibers (*9–11*). Their tolerance of arbitrary domains past a β-sheet–forming sequence makes them useful in biological signaling (*12, 13*). HA is a linear negatively charged macromolecule containing a disaccharide repeat unit of *N*-acetylglucosamine and glucuronic acid, present in mammalian extracellular matrix. When PA and HA solutions were combined in equal volumes, we observed the immediate formation of a solid membrane localized at the interface between the two liquids. If the denser HA solution is placed on top of the PA solution, the HA fluid sinks into the PA component, causing renewal of the liquid-liquid interface and resulting in continuous growth of membrane until the entire volume of HA solution is engulfed (Fig. 1A). This leads to the formation of a polymer-filled sac over periods of minutes to hours depending on the volume and density of the liquids used. Alternatively, closed sacs can be made instantly by injecting one solution directly into the bulk of the other, creating either HA-filled or PA-filled sacs. Other PAs tested led to similar results without obvious kinetic differences. However, as expected, the nature of the peptide sequence does affect the structural integrity of the membranes formed.

The instant initiation of ordered structures allows formation of self-sealing sacs (Fig. 1, B to D), films with tailorable size and shape (Fig. 1E), as well as continuous strings (Fig. 1F). Confocal microscopy confirmed the incorporation of both HA and PA components within the sac membranes (Fig. 1, G to I). Although formation of solids between oppositely charged macromolecules has been widely demonstrated (*14–17*), these systems commonly produce dense and disordered materials that are not permeable to large molecules (e.g., proteins) and are unstable in water without the use of cross-linking chemistry. Moreover, a large defect such as a hole or a crack in a solid made up of two oppositely charged polymers cannot be rapidly repaired by diffusion. The highly ordered materials described here are mechanically robust in both dry and hydrated states, can be permeable to proteins, and have the capability to self-seal defects instantly by self-assembly.

Recognizing the importance of electrostatic charge screening on the self-assembly of PA nanofibers, we investigated the effect of zeta potential in HA and PA solutions on membrane formation (*18*). Sac membranes with physical integrity formed only when both solutions had strong zeta potentials of opposite charge (Fig. 1J). The zeta potential determines the degree of stability of charged aggregates in solution, and in this case should correlate to the total electrostatic charge of molecules in the presence of counterions.

We investigated the microstructure of the PA-HA sac membranes as a function of time using electron microscopy (EM) (*18*). In the early stages of liquid-liquid contact, scanning electron micrographs reveal an amorphous layer (Fig. 2, A and D, region 1) adjacent to a layer of parallel fibers on the PA solution side (Fig. 2, A and D, region 2). We believe that rapid diffusion of the small PA molecules into the HA solution and electrostatic complexation of both molecules result in the formation of the amorphous zone. The parallel fiber region, which measures ~150 nm within 1 min of contact, is the result of self-assembly triggered by electrostatic screening of the amphiphiles by the negatively charged HA molecules near the interface. These early events that occur upon contact between the two liquids establish a diffusion barrier, which prevents the rapid mixing of the two miscible liquids. Ordered growth of nanofibers oriented perpendicular to the interface then forms a layer that measures ~1.5 µm after 30 min (Fig. 2B, region 3) and ~20 µm after 4 days of initial contact (Fig. 2C, region 3).

Transmission electron microscopy (TEM) of cross-sectional slices of a hydrated membrane sample (Fig. 2, E and F) (*18*) confirmed the morphologies observed by scanning electron microscopy (SEM) (Fig. 2D). TEM revealed the presence of the high–molar mass polymer throughout the

[1]Institute for BioNanotechnology in Medicine, Northwestern University, Chicago, IL 60611, USA. [2]3B's Research Group, Biomaterials, Biodegradables and Biomimetics, Department of Polymer Engineering, University of Minho, Braga, Portugal. [3]Department of Materials Science and Engineering, Northwestern University, Evanston, IL 60208, USA. [4]Department of Chemistry, Northwestern University, Evanston, IL 60208, USA. [5]Department of Medicine, Northwestern University, Chicago, IL 60611, USA.

*To whom correspondence should be addressed. E-mail: s-stupp@northwestern.edu